Microfluid Nanofluid (2015) 18:673–683
DOI 10.1007/s10404-014-1467-y

RESEARCH PAPER

On the droplet velocity and electrode lifetime of digital microfluidics: voltage actuation techniques and comparison

Cheng Dong · Tianlan Chen · Jie Gao · Yanwei Jia · Pui-In Mak · Mang-I Vai · Rui P. Martins

Received: 10 March 2014 / Accepted: 9 August 2014 / Published online: 19 August 2014

Abstract The distinct manageability of digital microfluidics (DMF) has rendered it a promising platform for building large-scale micro-reactors on a single chip for closed-loop automation. However, the limited velocity of the droplet transportation has hindered DMF from being utilized in high-throughput applications. This work investigates a control-engaged droplet actuation technique involving regular electronic hardware and computer-based software to simultaneously raise the velocity of the droplet transportation and elongate the electrode lifetime by lowering the root-mean-square value of the actuation voltage. The technique is based on a series of direct current (DC) pulses and multi-cycles of natural discharge coordinated with the droplet dynamic motions, facilitating real-time droplet position sensing. We found that the proposed technique was superior to both DC and AC in terms of the velocity. As to the electrode lifetime, all showed excellent performance under normal dielectric coating conditions, while AC (alternating current) performed the best under critical conditions. Altogether, this work exhibits a control-engaged electrode-driving scheme with a higher velocity and a longer lifetime compared with traditional DC actuation and for the first time provides a fundamental comparison among the techniques engaging different actuation signals.

Keywords Electrowetting-on-dielectric (EWOD) · Digital microfluidics · Transportation velocity · Electrode lifetime

1 Introduction

The introduction of electronic automation in the digital microfluidic (DMF) system (Chakrabarty et al. 2010; Gao et al. 2013; Shih et al. 2011) has highlighted it as a prospective platform for managing the intricacy of large-scale micro-reactors and underpinned a wide variety of on-chip biochemical applications such as immunoassays (Ng et al. 2012; Schertzer et al. 2012), DNA sample processing (Chang et al. 2006; Liu et al. 2008; Malic et al. 2009, 2011; Sista et al. 2008) and cell-based assays (Bogojevic et al. 2012; Eydelnant et al. 2012; Fan et al. 2008; Srigunapalan et al. 2012). Yet, to further position DMF in high-throughput applications such as cell sorting (Miller et al. 2011) and drug screening (Todd Thorsen and Quake 2002), the velocity of the droplet transportation ($v_{droplet}$) must be improved, without compromising its reliability and controllability. The velocity of the droplet transportation depends on the actuation voltage and the size of the droplet. Empirically, it barely reaches 2.5 mm/s at an actuation voltage below 20 V (Pollack et al. 2002).

Under the principle of electrowetting-on-dielectric (EWOD) (Fair 2007), the $v_{droplet}$ is determined by the following parameters: (1) the surface roughness and

Cheng Dong and Tianlan Chen have contributed equally to this work.

Rui P. Martins is on leave from Instituto Superior Técnico, University of Lisbon, Portugal.

Electronic supplementary material The online version of this article (doi:10.1007/s10404-014-1467-y) contains supplementary material, which is available to authorized users.

C. Dong · T. Chen · J. Gao · Y. Jia · P.-I. Mak (✉) · M.-I. Vai · R. P. Martins
State-Key Laboratory of Analog and Mixed-Signal VLSI and FST-ECE, University of Macau, Avenida Padre Tomás Pereira, Taipa, Macao, China
e-mail: pimak@umac.mo

hydrophobicity of a fabricated chip; (2) the hydrodynamics of a droplet which may contain chemical reagents or biological species with very different compositions, (3) the strength of the electric field for EWOD modulation and (4) the viscosity of the mediums causing drag forces that require high voltage to manipulate a droplet.

A few attempts have been made to address the problems based on either hardware or software improvements. Banerjee et al. (2011) have proposed a top-plate-less DMF system using coplanar electrodes to reduce the viscous dragging force between the liquid–solid interface. Brassard et al. (2008) have engineered the droplets with a water–oil core–shell structure to achieve a high v_{droplet}. Regrettably, both of them are vulnerable to sample contamination and evaporation that are intolerable for essential biochemical applications such as polymerase chain reaction (PCR) (Jia et al. 2013; Sista et al. 2008). Another hardware solution was proposed by Rajabi and Dolatabadi (2010), who tailored the electrode shape to boost up the v_{droplet}, at the expense of the droplet manageability. Instead of hardware modification, unguided DC-pulse train (Murran and Najjaran 2012b) could regulate the v_{droplet} for non-deformed droplet manipulation. However, in this case, the v_{droplet} was lower than that actuated by DC. Another work engaging residual charging (Noh et al. 2012) was capable of executing multi-droplet manipulation, but the waveform parameters were not studied for an optimum v_{droplet}.

Naturally, elevating the electrode-driving voltage could increase the electric field to accelerate the v_{droplet}. But it would compromise the chip lifetime due to dielectric breakdown (Fair 2007; Jebrail et al. 2012) and the cost of the electronics for high-voltage-tolerant design. To our knowledge, there is no electrode-driving technique that concurrently improves the v_{droplet} and elongates the electrode lifetime of a DMF chip.

Our previous work (Gao et al. 2013; Chen et al. 2014) on intelligent DMF has demonstrated a number of droplet-manipulation techniques. With an upgraded electronic feedback design, we managed to improve the v_{droplet} at a lower root-mean-square (RMS) value than the traditional approach by introducing a control-engaged electrode-driving technique named natural discharge after pulse (NDAP). In this paper, we will discuss NDAP in details and compare it with the widely used actuation signals in terms of the driving efficiency and the electrode lifetime.

By incorporating NDAP in our DMF system, we experimentally achieved 24.9 % lower RMS voltage, but 26.8 and 49.5 % higher v_{droplet} than the commonly used DC and AC actuation practices, respectively. The electrode lifetime of a chip actuated by NDAP was also improved almost threefold over that actuated by DC under critical dielectric coating conditions, while AC was superior to both NDAP and DC. Under the daily used coating conditions, all the three actuation signals have shown excellent performance in terms of the electrode lifetime. This work, together with our previous publications, should be valuable for scientists and engineers working on enhancing the throughput and the reliability of control-engaged DMF systems for automated applications.

2 Methods

2.1 Principle of natural discharge after pulse (NDAP)

DC (direct current) (Brassard et al. 2008; Cho et al. 2003; Damgaci and Cetiner 2013; Gong and Kim 2008; Malic et al. 2009; Pollack et al. 2002; Sen and Kim 2009; Witters et al. 2013) and AC (alternating current) (Abdelgawad et al. 2009; Barbulovic-Nad et al. 2008; Bavière et al. 2008; Jebrail and Wheeler 2009; Mousa et al. 2009; Nelson and Kim 2011; Shah et al. 2013; Zeng et al. 2013) are the common electrode-driving waveforms in EWOD-based DMF devices.

Murran and Najjaran (2012b) have studied the quasi-equilibrium status of a moving droplet, describing how the deformation and vibration of a droplet as well as the resistance force at the interfaces hinder the droplet movement. By investigating the characteristics (i.e., shape and contact angle) of a moving droplet, we invented a new control-engaged electrode-driving technique, NDAP, for a better v_{droplet} and a longer electrode lifetime.

As shown in Fig. 1, the initial high-level actuation was a t'_{α}-width DC with a peak value of u_{α}, providing the initial EWOD force to rapidly accelerate a droplet from still. Before the low-level actuation began, the actuation voltage dropped to a lower value due to the operation of the designed circuit described later.

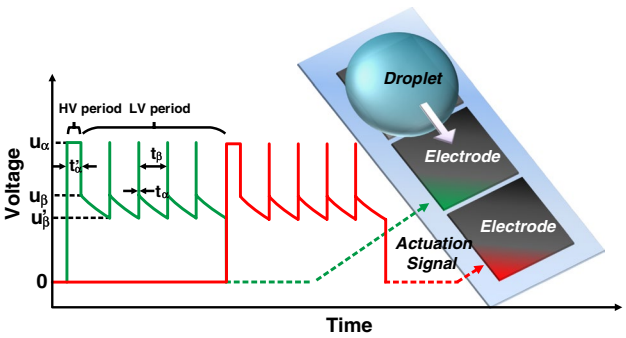

Fig. 1 Profiles of the electrode-driving signal, Natural Discharge after Pulse (NDAP), for a droplet moving across two electrodes. The high-voltage u_{α} (HV) period lasts a period of t'_{α}. The low-voltage (LV) period includes multi-cycles of natural discharges (t_{β}) and DC-pulse (t_{α}). u_{β} is the instantly decreased voltage when disconnecting an electrode. u'_{β} is the lowest voltage to maintain the movement of a droplet

When a droplet in run began to move, the high-level actuation was stopped by disconnecting the electrode from the power source but not grounded. During the natural discharge period, the residual charge on the electrode was still adequate for real-time sensing of the dynamic position of the droplet. The corresponding voltage on the electrode (u_{res}) was given by

$$u_{res} = u_\beta e^{-t/\tau}, \tag{1}$$

where u_β is the initial voltage of the discharge period, t is the elapsed time, and τ is the RC (Resistance–Capacitance) time constant, which is defined as

$$\tau = \mathrm{RC}. \tag{2}$$

During the natural discharge, a number of short (1 ms, t_α) recharging pulses were applied to the electrode to sustain the $v_{droplet}$ over a period of t_β, which could be managed by the control unit guiding the droplet movement till completion. The RMS voltage ($V_{RMS,\ discharge}$) of the discharge period was given by

$$V_{RMS,discharge} = \sqrt{\frac{1}{t_\beta}\int_0^{t_\beta} u_{res}^2 dt}. \tag{3}$$

Substituting Eqs. (1) and (2) into Eq. (3) yields

$$V_{RMS,discharge} = u_\beta \sqrt{\frac{RC}{2t_\beta}\left(1 - e^{-2\frac{t_\beta}{RC}}\right)}. \tag{4}$$

The expression inside the square root is always smaller than one. As a result, the RMS voltage is obviously lower than that of constant charging. In our case, RMS voltage of the whole actuation was up to 26.7 % lower than DC. The NDAP could also be applied to other DMF systems even without position sensing.

2.2 Real-time control-engaged electrode-driving scheme

Real-time feedback control is essential for optimizing the control signals. Fobel et al. (2013) have introduced the DropBot for precise control of the electrostatic driving force and the instantaneous measurement of the droplet velocity (Fobel et al. 2013; Shih et al. 2011, 2012, 2013). It is necessary to compensate the decrease in the driving voltage when measuring the electrical impedance during droplet transportation in DropBot. This would request a fine tune of the compensation circuit to adapt to a variety of DMF devices and driving signals. The feedback mechanism we used in this work was electrical capacitance-based sensing (Gao et al. 2013; Gong and Kim 2008; Murran and Najjaran 2012a; Ren et al. 2004; Schertzer et al. 2010), which could monitor the droplet location and track the droplet trajectory in real time without the need of calibration each time.

Our DMF prototype (Fig. 2a) consisted of two sub-modules: (1) Actuation signal generation module and (2) Real-time feedback acquisition module.

The actuation signal generation module featured 24 individual channels to drive the electrodes of the DMF chip. Each channel was equipped with two switches, one blocking/storage capacitor, C_b, and two fast switching diodes. To ensure the duration accuracy of the applied control signal, six high-voltage analog switch ICs (CPC7220) (each has eight switches) were utilized to save the turn-on/off time (<5 μs), which was much faster than the relays (1 ms) used in our previous work. Since there were two voltage domains, C_b was essential to isolate the feedback module (0–3.3 V) from the control module (0–50 V) and served as a charge keeper after disconnecting the electrode from the voltage source, for droplet positioning.

During the DC pulsing (initial one or recharging ones), C_b and $C_{droplet}$ were to be charged at different voltage values (e.g., ~11 and ~15 V, when u_α was set to 15 V). Thus, the natural discharge process after DC pulsing would pass through two phases. The first was fast given the small value of $C_{droplet}$ (~10 pF). The second was much slower as it was dominated by C_b (~450 nF). Since the first discharge period minimally affected the circuit, our later discussions would focus on the dominating second discharge. The two diodes were to protect the low-voltage feedback module from overdriving during the transients of capacitor between charging and discharging.

The feedback module featured two multiplexers and a ring oscillator. The multiplexers made it possible to use a single ring oscillator (a Schmitt trigger and a resistor) to quickly scan all electrodes, generating a set of capacitance-derived frequency data to evaluate the real-time droplet position. The analog multiplexer also acted as a resistor (275 kΩ) connected to the ground for the natural discharge. Since $C_{droplet}$ dominated the equivalent capacitance of the ring oscillator, the responded frequency data represented accurately the variation of the electrode capacitance during the droplet transportation.

An FPGA chip was used in our control system. Its high-efficient programmable gate array helped to precisely manage the control PCB and generate the requested actuation signal. Control parameters such as actuation electrodes, charging duration and signal frequency could be set in the computer-based software and sent to the FPGA to process.

The feedback data were digitalized and organized by the FPGA in real time with a digital frequency counter. Once all the 24 electrodes' capacitances were measured, the data would be transferred to the computer via a serial port for calculation and determination of the response.

3 Experiments

3.1 Device fabrication

The DMF devices were fabricated and assembled following the protocols described previously (Gao et al. 2013). A drop of aqueous solution (~0.5 μL) immersed in silicon oil (1 cSt) (Sigma-Aldrich, MO) or hexadecane (3.34 cSt) (Sigma-Aldrich, MO) was sandwiched by a bottom glass and a top Indium Tin Oxide (ITO, Kaivo Optoelectronic) glass with a 0.25-mm spacer. Electrodes (1 mm × 1 mm) patterned on the bottom glass were separated from each other with a 0.01 mm gap. A dielectric layer of Ta_2O_5 (250/50 nm) was coated on the electrodes followed by a layer of Parylene C (480 nm) (Galxyl) and then a layer of Teflon AF 1600 (100 nm) (DuPont). Silane A-174 (Momentive Performance Materials) was utilized to improve the bonding between the Ta_2O_5 and Parylene C layers. The top ITO glass (Kaivo, ITO-P001) was coated with a layer of 100 nm Teflon AF 1600.

3.2 Experimental setup

Figure 2b, c show the experimental setup. A red LED was placed on chip next to the electrode matrix (Fig. 2d) and controlled by the FPGA. It lighted up when any of the electrodes was connected to the power source. The chip was put under a microscope and monitored with a high-speed camera (Nikon V2), which has a maximum frame rate up to 1,200 frames/second (resolution 320 × 120 pixels). The movement of the droplet was captured in every 0.83 ms. The top glass was grounded to provide an electric field over the droplet.

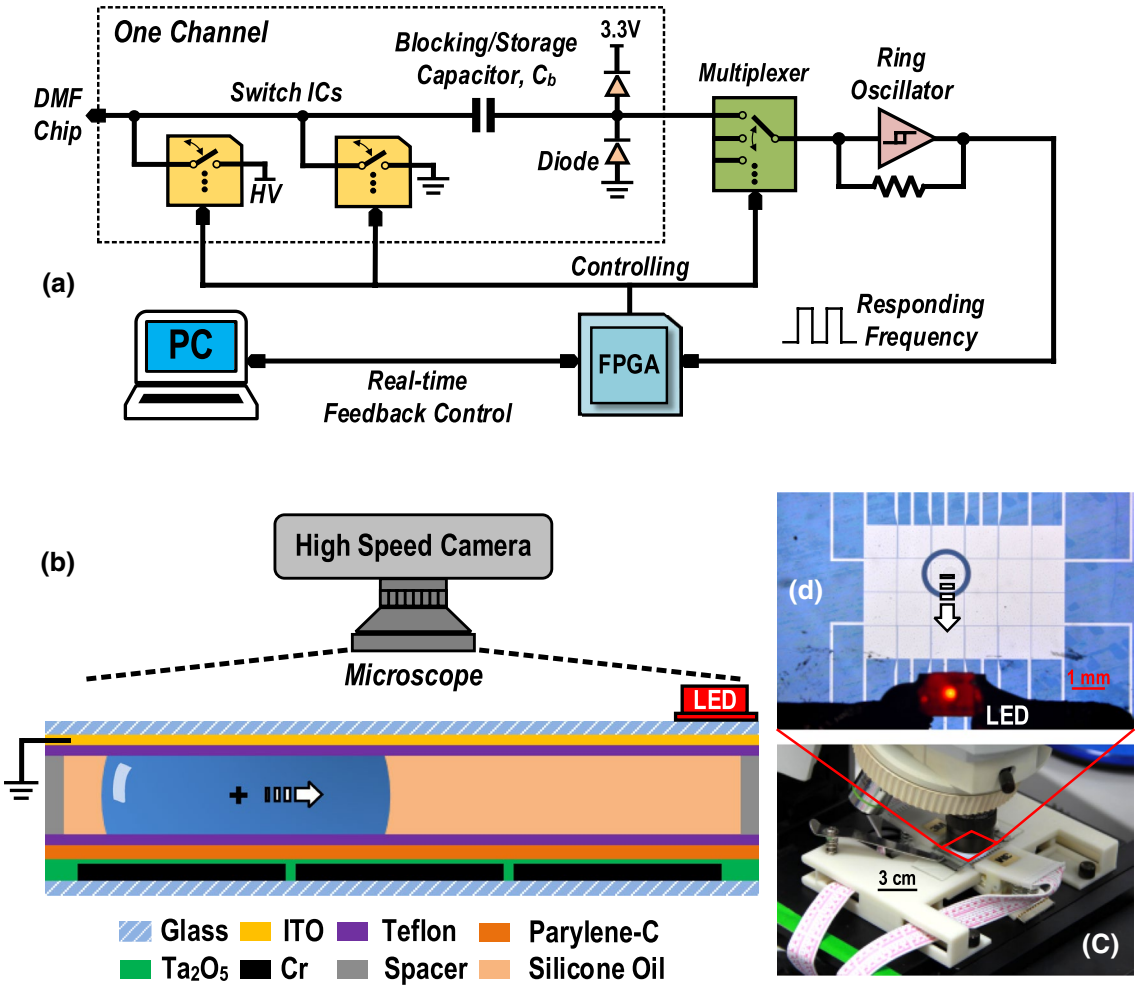

Fig. 2 Experimental setup for measuring the droplet dynamics under different electrode-driving signals: **a** Schematics of the real-time feedback-control system. Feedback of the droplet position is acquired by the FPGA based on the responding frequency of a ring oscillator. A computer-based software controls the switches through the FPGA according to the feedback data. **b** DMF chip and setup of the observation system. An on-chip LED lights up when any of the electrodes is connected to the power source. A camera is mounted onto the microscope for video-recording of the droplet movement. **c** Installation of the DMF chip. **d** An example image of the DMF chip captured by the camera

3.3 Data analysis

Individual frames extracted from videos were analyzed using an image processing software, *Image J*. The centroid of the droplet was obtained as the center of mass of an irregular shape and was used as the droplet position for calculating the transportation velocity. As the centroid was calculated from the droplet's two-dimensional area, the velocity would reflect the deformation of the droplet during transportation. The droplet morphometry and velocimetry were analyzed the same way as Basu (2013). The appearance of the red light in the image marked the exact frames where the charging started and ended. As such, all the analysis could be exactly over the period when the power was on. Details of the data analysis can be found in "Video Data Processing" section of ESM_1.

4 Results and discussion

4.1 Dynamics of droplet movement

The transportation of a droplet from one electrode to another is not linear. Bavière et al. (2008) have described the droplet transportation between electrodes in three phases: Phase I (only the leading edge moves, while the trailing edge is still pinned), Phase II (both the leading and trailing edges move with great different velocities), and Phase III (both edges move with a similar velocity).

We analyzed our videos (one of them can be found in ESM_2) and determined the boundaries of the three phases described by Bavière et al. (2008). Figure 3a shows the droplet movement from 0 to 230 ms, where the first row focuses on the very beginning of charging and the second row shows the rest. As soon as the driving signal was applied, Phase I started instantly, resulting in a shape deformation of the droplet where the front edge became thinner and the trailing edge stayed pinned. Phase II began at around 10 ms when the trailing edge unpinned and started to catch up the leading edge, as shown in Fig. 3a.

It is hard to find the beginning time of phase III by observing the video images. Here we present a convenient method to determine the boundaries of the three phases from the instantaneous velocity of a droplet, as shown in Fig. 3b. The instantaneous velocity was calculated based on the movement of the droplet centroid, and thus, the conformation change of the droplet would be reflected on the velocity. As shown in Fig. 3b, there was a sudden velocity change from 0 to 3 mm/s at the moment when the power was applied. This was due to the deformation of the droplet in Phase I (Frame A in Fig. 3a and point A in Fig. 3b). For the same reason, when the trailing edge started to move,

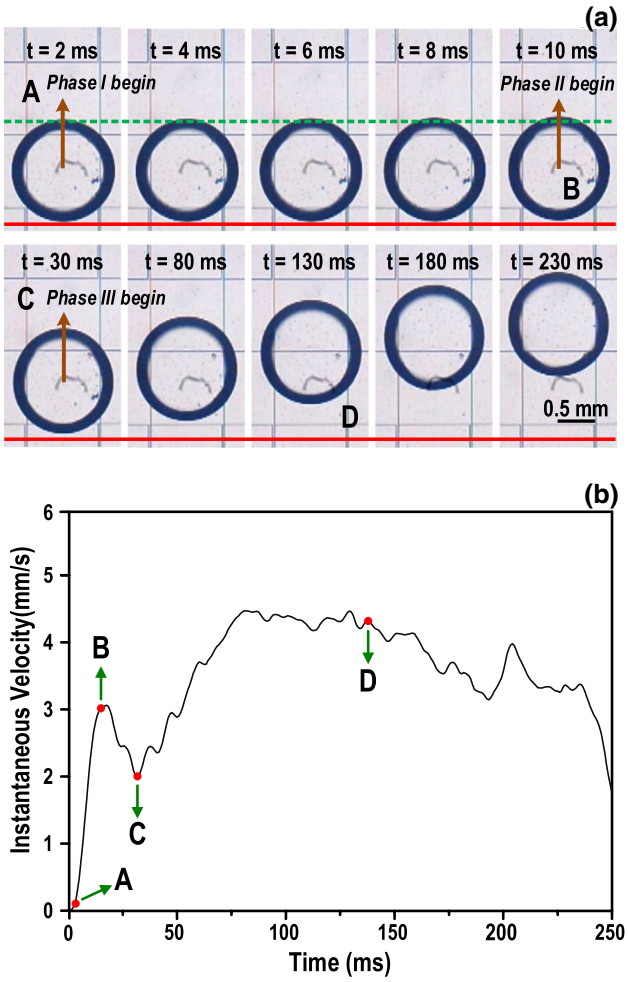

Fig. 3 Phase analysis of the droplet movement under a 15 V_{RMS} DC signal: **a** Droplet dynamic from 0–230 ms. Phase I started immediately when the power was applied. Frames *A*, *B*, *C* and *D* show the beginnings of Phase *I*, *II*, *III* and the moment when the centroid of the droplet reaches the edge of the target electrode. **b** The instantaneous velocity of a droplet moving across an electrode driven by DC. Points *A*, *B*, *C* and *D* correspond to frames *A*, *B*, *C* and *D* in (**a**), respectively

there would be another steep change in the droplet conformation, which would cause a decrease in the calculated velocity. Point B at ~10 ms in Fig. 3b marked the beginning of Phase II, which was consistent with that obtained from Fig. 3a. When the trailing edge caught up the front edge and kept the conformation of the droplet stable, Phase III started and the instantaneous velocity would increase smoothly with the continuous driving signal application. Point C in Fig. 3b marked the start of Phase III at around 30 ms. These observations of the three phases were qualitatively consistent with that observed by Bavière et al. (2008). Note that after 130 ms, Point D, the droplet velocity started to decline. By investigating the video, we found that this was the time when the centroid of the droplet reached the lower edge of the target electrode as shown in Fig. 3a.

The EWOD force applied at the contact line. When the centroid of the droplet passed the edge, the EWOD force on the rear part would be a dragging force instead of a driving force, which caused the droplet to slow down. There was another sudden velocity change close to the end of the transportation. It happened when the leading edge of the droplet reached the rim of the target electrode and stopped moving forward. Again, the sudden conformation change would be reflected on the velocity. After that, the velocity dropped quickly. Hence, by studying the instantaneous velocity of a droplet, we could obtain the dynamics of the droplet transportation, which was crucial in optimizing our NDAP signal analyzed as follows.

4.2 Driving efficiency of NDAP

In general, increasing the RMS value of the actuation signal is an effective way to raise the $v_{droplet}$ on the DMF chip. Nevertheless, chip aging and breakdown problems arise with a high RMS actuation voltage. In order to maintain the $v_{droplet}$ while lowering the RMS voltage, the driving efficiency of the actuation signal would have to be enhanced.

To date, there has been no report describing and comparing the efficiencies of different electrode-driving signals. In this work, we introduce an NDAP signal with a scope of reducing the RMS voltage while improving the $v_{droplet}$. To assess the performance of NDAP, we for the first time compared the $v_{droplet}$ of a DI water droplet immersed in silicon oil, moving across an electrode driven by NDAP with that driven by DC. The charging time of DC was empirically fixed at 300 ms to complete the transportation. NDAP was executed by the feedback-control unit. The natural discharge could be multi-cycled to complete the transportation.

As illustrated in Fig. 4a, a DC signal with a 15 V_{RMS} gave an average velocity of 3.73 mm/s. This velocity was slightly dependent on the size of the droplet. With the NDAP signal, the average velocity increased dramatically from 2.74 mm/s with a $t_{\alpha}^{'}$ of 1 ms, to 4.18 mm/s with a $t_{\alpha}^{'}$ of 13 ms. The RMS value of 13 ms NDAP was only 10.87 V, 73 % of that of DC. However, the average velocity under this condition was even higher than that of the DC driving signal. Considering the droplet dynamics during the transportation, we suspected that when the first pulse duration was less than needed to overcome Phase I, the driving force would be inadequate to move the droplet at a high speed, although the natural discharge in NDAP may still pull the droplet forward. Therefore, the average transporting efficiency would remain low. However, if the first pulse in NDAP made the droplet move into Phase II or III, the whole droplet started to move in a stretching conformation. The retreat of the force would cause the droplet to relax and return to a round shape as much as possible. The rounded shape would maximize the driving force efficiency (Ren et al. 2002), which as a consequence would speed up the droplet transportation driven by NDAP to even faster than by DC. The natural discharge period in NDAP was critical for the real-time droplet position feedback, as the charging to an electrode had to be disconnected for a sensing signal to be sent to the same electrode.

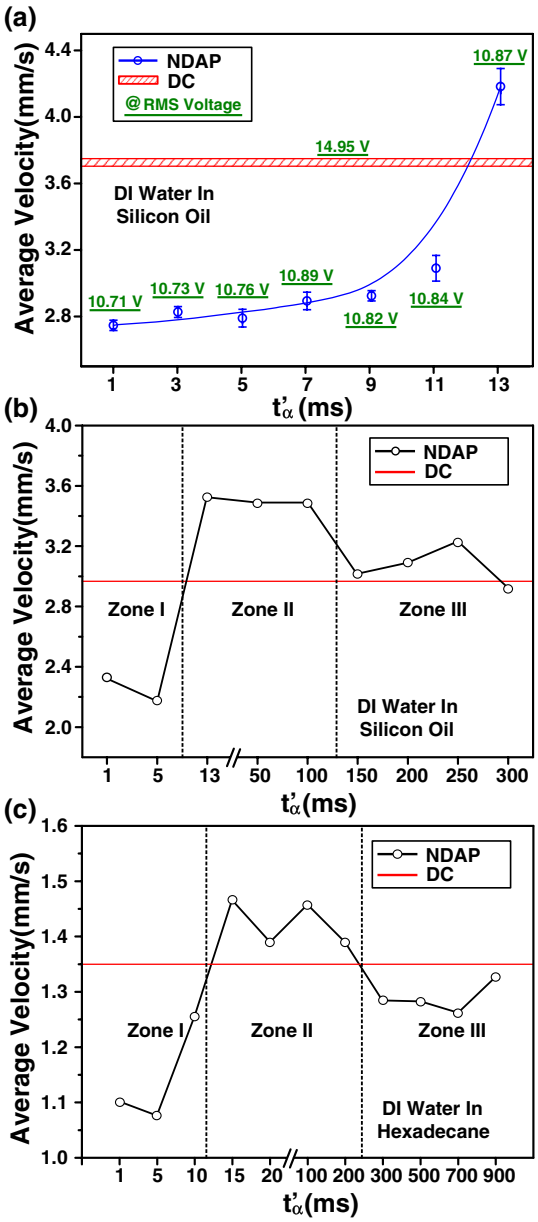

Fig. 4 Average velocity analysis under NDAP signal in comparison of DC signal: **a** the average velocities of a droplet driven by NDAP signals with different $t_{\alpha}^{'}$. The corresponding RMS voltages are shown in the figure. **b** The average velocity of a DI water droplet in silicon oil driven by NDAP with a $t_{\alpha}^{'}$ changing from 1 to 300 ms. *Zone I*, *II* and *III* mark the regions where NDAP performs worse than, better than or as good as DC actuation signal. **c** The average velocity of a DI water droplet in hexadecane driven by NDAP with a $t_{\alpha}^{'}$ changing from 1 to 900 ms

Table 1 Phase II begin time for different conditions

u_α (V)	Phase II begin time (ms)		
	DI water in silicon oil (1.0 cSt)	DI water with 8 μm particle in silicon oil (1.0 cSt)	DI water in hexadecane (3.34 cSt)
15	10.00	10.83	15.00
20	8.33	8.33	12.50
25	7.50	8.33	11.67
30	7.50	8.33	11.67
35	7.50	7.50	11.67

In order to verify our hypothesis, we investigated the average velocity of droplet transportation with t_α' from 1 to 300 ms and compared it with that driven by a DC signal. As shown in Fig. 4b, when t_α' was <10 ms, which was the boundary of the Phase I and Phase II, the average velocity was less than that driven by DC. This range was labeled as zone I, where the transporting efficiency remained low. However, when $t_\alpha'$was between 10 and 130 ms (zone II), the average velocity reached ~3.5 mm/s, which was 20.6 % higher than that of DC (2.9 mm/s). A further increase of t_α' did not add more value. When t_α' was larger than 130 ms (zone III), the velocity returned back to that of DC. As we have discussed, 130 ms was the time when the centroid of the droplet got onto the second electrode. Under this condition, NDAP showed no more improvement in the velocity of droplet transportation because its high driving efficiency worked on both the front and trailing edges. The force on the trailing edge was actually a dragging force. Balancing the velocity and electrode lifetime, we concluded that using a t_α' just into the boundary of Phase II would be the optimized NDAP signal.

The beginning of Phase II may vary with different chemical or biological systems, which would require a calibration for each case. We tested the start point of Phase II with different driving voltages, different immerse oils and different sample components to investigate the variations.

As shown in Table 1, rising u_α from 15 to 25 V shortened the Phase I period from 10 to 7.5 ms for a DI water droplet in silicon oil (1 cSt). Further increase in driving voltage did not affect the phase behavior of the droplet. We also studied a water droplet dispersed with stabilized 8 μm polystyrene particles (Nano Micro. Ltd) to mimic the biological samples with cells in the droplet. The phase behavior stayed similar to that of pure deionized water. The beginning of Phase II took place 2.5 ms earlier with a higher voltage than a just adequate driving voltage.

For some biological applications which need to heat up the samples, such as PCR, the high evaporation rate of the silicon oil (1 cSt) makes it inappropriate as an immerse oil. Replacing it with a thermal stable but more viscous oil is inevitable. We investigated the phase behavior of a water droplet in hexadecane (3.34 cSt) with u_α set to 20 V to see if that would cause a necessary recalibration of the system. As shown in Table 1, Phase II started at 12.5 ms, which was about 50 % later than that in the silicon oil. However, the zone I to zone III for DI water droplet in hexadecane (Fig. 4c) was still consistent with that in silicon oil, matching its beginning of Phase II (the boundary of zone I and II) and the moment that the centroid of the droplet reached the edge of the target electrode (the boundary of zone II and III). This further confirmed our hypothesis.

We admit that the phase behavior of a droplet varied in a range of 4 ms in different immerse oils. However, compared with the range of zone II which was up to 130 ms in silicon oil or 250 ms in hexadecane, the off-optimization of this 4 ms is negligible. Conservatively, one could use the optimized t_α' at a low voltage for all NDAP signals on aqueous droplets. As such, recalibration of the system to optimize t_α' for different applications is likely unnecessary.

The duration of t_α' was the dominant parameter in optimizing the driving efficiency of NDAP. Only when the t_α' was long enough to make the droplet enter the dynamic phase II but not long enough to drive the centroid of the droplet passing the edge of the second electrode would make the droplet move faster than actuated by DC. u_α was kept as low as possible for a low RMS value while still maintaining the movement of the droplet. u_β was the unchangeable voltage after instant discharge when disconnecting an electrode. It was determined by the electronic circuit discussed in Sect. 2.2. u_β' was set as the lowest voltage to maintain the droplet movement. A voltage below this value would cause the droplet stop moving and a higher value would raise the whole RMS value during the charging period. t_α was again set as short as possible and t_β was the time for the system to reach u_β' after disconnecting an electrode. The optimization of all these parameters was pretty limited by the system, and not necessary.

4.3 Performance comparison among NDAP, DC and AC actuation signals

The above comparisons of performance were all between NDAP and DC actuation signals as NDAP was DC-based. However, many research groups have demonstrated the

superiority of AC actuation compared with DC for its reliability and reproducibility. In order to further test the performance of our new techniques, we modified our signal generating system and reran the experiments for evaluating the velocity of droplet transportation and the electrode lifetime of a chip.

In the experiments of velocity determination, a droplet of DI water (0.5 μL) was transported from one electrode to the next under different actuation signals. The same electrodes were used for running DC, AC and NDAP. AC signal used in experiments was symmetric square wave. The peak values of all the three signals were fixed at 15 V. In NDAP signal, 15 ms $t_{\alpha}^{'}$ was used for the best driving performance. The charging of AC or DC was sustained till the movement had been completed. Therefore, the RMS voltages of AC, DC and NDAP were 15, 15 and 11.27 V, respectively. The frequency of the AC signal was set at 1 kHz, which was a widely used frequency in literatures.

As shown in Fig. 5a, the droplet actuated by the NDAP signal reached the target electrode in the shortest time (~250 ms), while DC signal took a longer time (~300 ms) and AC signal took the longest time (~400 ms) to complete the droplet transportation.

A droplet running across an eight-electrode straight array was monitored to obtain the average velocities driven by DC, AC and NDAP. The charging duration of DC and AC was empirically optimized at 300 and 400 ms, respectively, to complete the movement from one electrode to the next. The average velocities were calculated over the droplet movement period disregarding whether the actuation signal stopped or not.

As shown in Fig. 5b, NDAP reached a velocity of 4.4 mm/s while DC gave 3.4 mm/s and AC only reached 2.9 mm/s. NDAP raised the velocity by 26.8 and 49.5 % when compared to DC and AC, respectively. This result could be explained by the dielectric permittivity, which is related to the type and the structure of a material. The as-deposited Ta_2O_5 thin films used in this work were rapidly thermal annealed at 400 °C for 10 min, giving the film in amorphous state. The reduction of the dielectric permittivity of such film was very sharp from static electric field to 1 kHz alternative electric field (Sethi et al. 2011; Shibata 1996; Wei et al. 2011). Consequently, the electrowetting force induced by the DC electric field could be higher than that of AC, as well as the actuation velocity. Furthermore, a higher DC voltage would result in a higher actuation velocity. As long as the chip was sustainable, switching from DC to NDAP would always improve the droplet transportation efficiency.

Since NDAP had a low RMS voltage, we expected that the electrode lifetime with NDAP would be longer than both DC and AC. To test this hypothesis, we shuttled a droplet between two adjacent electrodes driven by DC, AC and NDAP. The charging duration of DC and AC was set empirically at 250 and 400 ms. The electrode lifetime was determined when an electrode breakdown was monitored (Fig. 6a), even though the droplet could still move in some cases. The dielectric layer was normally 250 nm in the experiments in this paper. As shown in Fig. 6b, the electrode did not show any sign of breakdown after 10,000 shuttles for all the three actuation signals under normal dielectric coating conditions.

In order to touch the limit of the electrode lifetime, we coated a batch of chips with a critical thickness of 50 nm of dielectric layer, which were prone to breakdown. As shown in Fig. 6b, NDAP had an electrode lifetime about three times longer than that of DC with a value of 200 and 63 shuttles, respectively. This could be attributed to the lower RMS value of NDAP. But unexpectedly, DMF chips

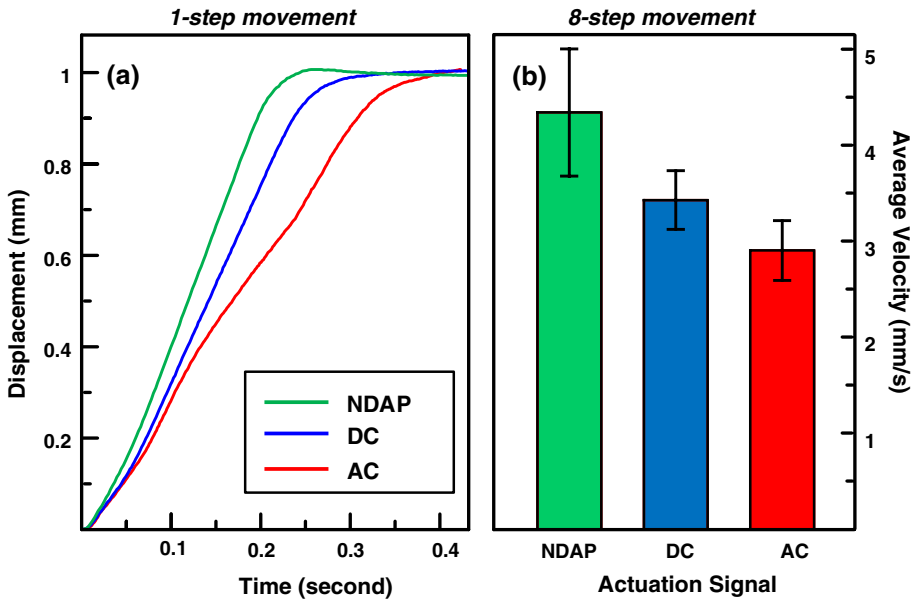

Fig. 5 Velocity comparisons of the three different actuation signals DC, AC and NDAP: **a** Typical displacement curves of a droplet moving across one electrode driven by DC, AC and NDAP. **b** The average velocity of a droplet moving across an eight-electrode straight array. Each experiment was repeated ten times

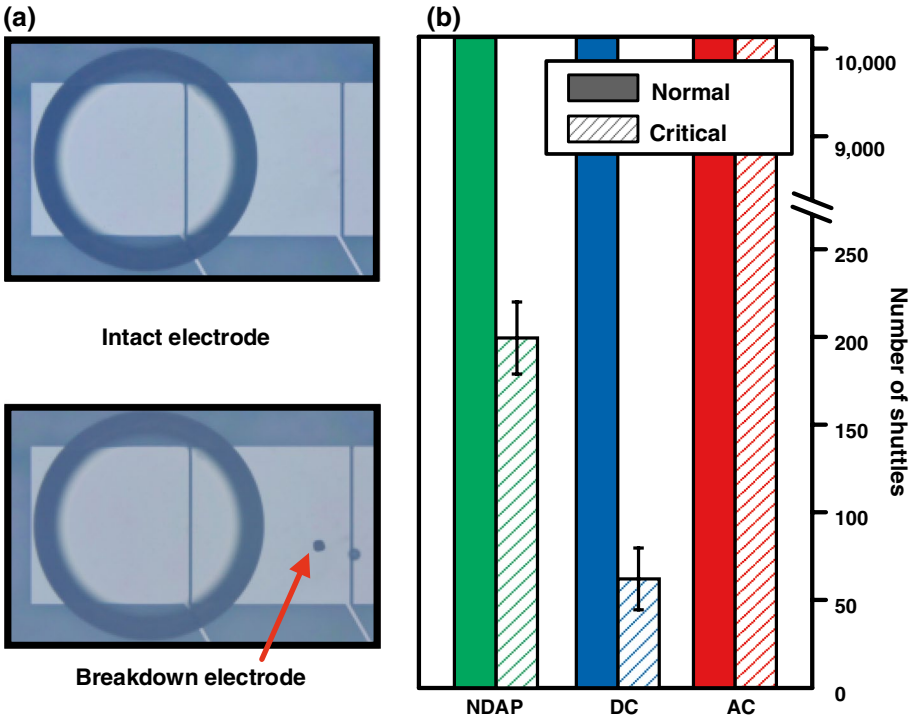

Fig. 6 The comparison of the electrode lifetime under the three actuation signals DC, AC and NDAP. **a** Photographs of an intact electrode and a breakdown electrode. **b** Number of shuttles a droplet has completed before the electrode breakdown under the normal dielectric coating (250 nm Ta_2O_5 layer) and the critical dielectric coating (50 nm Ta_2O_5 layer) conditions

actuated by AC were still robust even under those critical coating conditions. This may be attributed to the defects or impurities in the thin layer of the dielectric material. For a dielectric layer as thin as 50 nm, the occurrence of defects and impurities dramatically increase. The presence of defects at the metal surface lowers the breakdown potential at these defects (Albella et al. 1991), causing easier break down of the dielectric layer. Defects and impurity also induce charge trapping. According to the Poole–Frenkel emission conduction mechanism, the trapped electrons could escape by thermal emission and form current due to electrons "jumping" from trap to trap. Charges trapped in dielectric layer intend to stay inside when unipolar electrical field, such as DC and NDAP, are applied. In contrast, the trapped charge would be released in alternative electric field when switching the direction. It has been found that the charge trapping-related leakage current is more obvious for DC-based signal than AC, resulting in a field stress in DC and NDAP and shortening the electrode lifetime. A video of these experiments can be found in ESM_3.

However, in the DMF community, people always coat a chip with thick enough dielectric layer for a robust performance. Therefore, the lifetime of all the three actuation signals is same good in real-life usage. Nevertheless, under some circumstances when droplet contains charged materials such as protein or DNA, DC-based signals with the same polarity of the charge as the sample would be desired in order to eliminate the adhesion of those materials to the electrodes. In those cases, NDAP would be preferred in the view of both the velocity and the electrode lifetime.

5 Conclusions

By matching the droplet dynamics with the strength and duration of the applied electric field, we have speeded up the droplet movement to a higher value than DC and AC actuation signals by incorporating feedback control with NDAP as the electrode-driving techniques. The electrode lifetime comparison under DC, AC and NDAP has revealed that AC is the safest actuation signal, and NDAP is superior to DC. The entire NDAP scheme involves only regular electronics and software programming, being highly upgradable for the following-up research, customizable to other applications, and easily repeatable by other research groups. The thorough comparisons on the performance of NDAP with currently widely used DC and AC signals have established a clear guideline and provided another option for choosing the right actuation signal in different applications, such as DNA analysis and protein manipulations.

Acknowledgments This work was financially supported by the University of Macau and Macao Science and Technology Development Fund (FDCT) under No. 033/2011/A2 and State Key Lab Fund.

References

Abdelgawad M, Watson MWL, Wheeler AR (2009) Hybrid microfluidics: a digital-to-channel interface for in-line sample processing and chemical separations. Lab Chip 9:1046–1051. doi:10.1039/b820682a

Albella JM, Montero I, Martinez-Duart JM, Parkhutik V (1991) Dielectric breakdown processes in anodic Ta205 and related oxides. J Mater Sci 26:3422–3432. doi:10.1007/BF00557127

Banerjee AN, Qian SZ, Joo SW (2011) High-speed droplet actuation on single-plate electrode arrays. J Colloid Interface Sci 362:567–574. doi:10.1016/j.jcis.2011.07.014

Barbulovic-Nad I, Yang H, Park PS, Wheeler AR (2008) Digital microfluidics for cell-based assays. Lab Chip 8:519–526. doi:10.1039/b717759c

Basu AS (2013) Droplet morphometry and velocimetry (DMV): a video processing software for time-resolved, label-free tracking of droplet parameters. Lab Chip 13:1892–1901. doi:10.1039/C3LC50074H

Bavière R, Boutet J, Fouillet Y (2008) Dynamics of droplet transport induced by electrowetting actuation. Microfluid Nanofluidics 4:287–294. doi:10.1007/s10404-007-0173-4

Bogojevic D, Chamberlain MD, Barbulovic-Nad I, Wheeler AR (2012) A digital microfluidic method for multiplexed cell-based apoptosis assays. Lab Chip 12:627–634. doi:10.1039/c2lc20893h

Brassard D, Malic L, Normandin F, Tabrizianc M, Veres T (2008) Water-oil core-shell droplets for electrowetting-based digital microfluidic devices. Lab Chip 8:1342–1349. doi:10.1039/b803827a

Chakrabarty K, Fair RB, Zeng J (2010) Design tools for digital microfluidic biochips: toward functional diversification and more than moore. IEEE Trans Comput-Aided Des Integr Circuits Syst 29:1001–1017. doi:10.1109/tcad.2010.2049153

Chang YH, Lee GB, Huang FC, Chen YY, Lin JL (2006) Integrated polymerase chain reaction chips utilizing digital microfluidics. Biomed Microdevices 8:215–225. doi:10.1007/s10544-006-8171-y

Chen T, Dong C, Gao J, Jia Y, Mak PI, Vai MI, Martins RP (2014) Natural discharge after pulse and cooperative electrodes to enhance droplet velocity in digital microfluidics. AIP Adv 4. doi:10.1063/1.4873407

Cho SK, Moon HJ, Kim CJ (2003) Creating, transporting, cutting, and merging liquid droplets by electrowetting-based actuation for digital microfluidic circuits. J Microelectromech Syst 12:70–80. doi:10.1109/jmems.2002.807467

Damgaci Y, Cetiner BA (2013) A frequency reconfigurable antenna based on digital microfluidics. Lab Chip 13:2883–2887. doi:10.1039/c3lc50275a

Eydelnant IA, Uddayasankar U, Li BY, Liao MW, Wheeler AR (2012) Virtual microwells for digital microfluidic reagent dispensing and cell culture. Lab Chip 12:750–757. doi:10.1039/c2lc21004e

Fair RB (2007) Digital microfluidics: is a true lab-on-a-chip possible? Microfluid Nanofluidics 3:245–281. doi:10.1007/s10404-007-0161-8

Fan SK, Huang PW, Wang TT, Peng YH (2008) Cross-scale electric manipulations of cells and droplets by frequency-modulated dielectrophoresis and electrowetting. Lab Chip 8:1325–1331. doi:10.1039/b803204a

Fobel R, Fobel C, Wheeler AR (2013) DropBot: An open-source digital microfluidic control system with precise control of electrostatic driving force and instantaneous drop velocity measurement. Appl Phys Lett 102 doi:10.1063/1.4807118

Gao J et al (2013) An intelligent digital microfluidic system with fuzzy-enhanced feedback for multi-droplet manipulation. Lab Chip 13:443–451. doi:10.1039/c2lc41156c

Gong J, Kim CJ (2008) All-electronic droplet generation on-chip with real-time feedback control for EWOD digital microfluidics. Lab Chip 8:898–906. doi:10.1039/b717417a

Jebrail MJ, Wheeler AR (2009) Digital microfluidic method for protein extraction by precipitation. Anal Chem 81:330–335. doi:10.1021/ac8021554

Jebrail MJ, Bartsch MS, Patel KD (2012) Digital microfluidics: a versatile tool for applications in chemistry, biology and medicine. Lab Chip 12:2452–2463. doi:10.1039/c2lc40318h

Jia YW, Mak PI, Massey C, Martins RP, Wangh LJ (2013) Construction of a microfluidic chip, using dried-down reagents, for LATE-PCR amplification and detection of single-stranded DNA. Lab Chip 13:4635–4641. doi:10.1039/C3LC51049B

Liu YJ, Yao DJ, Lin HC, Chang WY, Chang HY (2008) DNA ligation of ultramicro volume using an EWOD microfluidic system with coplanar electrodes. J Micromech Microeng 18 doi:10.1088/0960-1317/18/4/045017

Malic L, Veres T, Tabrizian M (2009) Biochip functionalization using electrowetting-on-dielectric digital microfluidics for surface plasmon resonance imaging detection of DNA hybridization. Biosens Bioelectron 24:2218–2224. doi:10.1016/j.bios.2008.11.031

Malic L, Veres T, Tabrizian M (2011) Nanostructured digital microfluidics for enhanced surface plasmon resonance imaging. Biosens Bioelectron 26:2053–2059. doi:10.1016/j.bios.2010.09.001

Miller EM, Ng AHC, Uddayasankar U, Wheeler AR (2011) A digital microfluidic approach to heterogeneous immunoassays. Anal Bioanal Chem 399:337–345. doi:10.1007/s00216-010-4368-2

Mousa NA et al. (2009) Droplet-scale estrogen assays in breast tissue, blood, and serum. Sci Transl Med 1 doi:10.1126/scitranslmed.3000105

Murran MA, Najjaran H (2012a) Capacitance-based droplet position estimator for digital microfluidic devices. Lab Chip 12:2053–2059. doi:10.1039/c2lc21241b

Murran MA, Najjaran H (2012b) Direct current pulse train actuation to enhance droplet control in digital microfluidics. Appl Phys Lett 101:144102. doi:10.1063/1.4756914

Nelson WC, Kim CJ (2011) Monolithic fabrication of EWOD chips for picoliter droplets. J Microelectromech Syst 20:1419–1427. doi:10.1109/jmems.2011.2167673

Ng AHC, Choi K, Luoma RP, Robinson JM, Wheeler AR (2012) Digital microfluidic magnetic separation for particle-based immunoassays. Anal Chem 84:8805–8812. doi:10.1021/ac3020627

Noh JH, Noh J, Kreit E, Heikenfeldb J, Rack PD (2012) Toward active-matrix lab-on-a-chip: programmable electrofluidic control enabled by arrayed oxide thin film transistors. Lab Chip 12:353–360. doi:10.1039/C1LC20851A

Pollack MG, Shenderov AD, Fair RB (2002) Electrowetting-based actuation of droplets for integrated microfluidics. Lab Chip 2:96–101. doi:10.1039/b110474h

Rajabi N, Dolatabadi A (2010) A novel electrode shape for electrowetting-based microfluidics. Colloid Surf A-Physicochem Eng Asp 365:230–236. doi:10.1016/j.colsurfa.2010.01.039

Ren H, Fair RB, Pollack MG, Shaughnessy EJ (2002) Dynamics of electro-wetting droplet transport. Sens Actuator B-Chem 87:201–206. doi:10.1016/s0925-4005(02)00223-x

Ren H, Fair RB, Pollack MG (2004) Automated on-chip droplet dispensing with volume control by electro-wetting actuation and capacitance metering. Sens Actuator B-Chem 98:319–327. doi:10.1016/j.snb.2003.09.030

Schertzer MJ, Ben-Mrad R, Sullivan PE (2010) Using capacitance measurements in EWOD devices to identify fluid composition and control droplet mixing. Sens Actuator B-Chem 145:340–347. doi:10.1016/j.snb.2009.12.019

Schertzer MJ, Ben Mrad R, Sullivan PE (2012) Automated detection of particle concentration and chemical reactions in EWOD devices. Sens Actuator B-Chem 164:1–6. doi:10.1016/j.snb.2012.01.027

Sen P, Kim CJ (2009) A fast liquid-metal droplet microswitch using EWOD-driven contact-line sliding. J Microelectromech Syst 18:174–185. doi:10.1109/jmems.2008.2008624

Sethi G, Bontempo B, Furman E, Horn MW, Lanagan MT, Bharadwaja SSN, Li J (2011) Impedance analysis of amorphous and polycrystalline tantalum oxide sputtered films. J Mater Res 26:745–753. doi:10.1557/jmr.2010.77

Shah GJ, Ding HJ, Sadeghi S, Chen SP, Kim CJ, van Dam RM (2013) On-demand droplet loading for automated organic chemistry

on digital microfluidics. Lab Chip 13:2785–2795. doi:10.1039/c3lc41363b

Shibata S (1996) Dielectric constants of Ta2O5 thin films deposited by r.f. sputtering. Thin Solid Films 277:1–4. doi:10.1016/0040-6090(95)08234-4

Shih SCC, Fobel R, Kumar P, Wheeler AR (2011) A feedback control system for high-fidelity digital microfluidics. Lab Chip 11:535–540. doi:10.1039/c0lc00223b

Shih SCC et al (2012) Dried blood spot analysis by digital microfluidics coupled to nanoelectrospray ionization mass spectrometry. Anal Chem 84:3731–3738. doi:10.1021/ac300305s

Shih SCC, Barbulovic-Nad I, Yang XN, Fobel R, Wheeler AR (2013) Digital microfluidics with impedance sensing for integrated cell culture and analysis. Biosens Bioelectron 42:314–320. doi:10.1016/j.bios.2012.10.035

Sista R et al (2008) Development of a digital microfluidic platform for point of care testing. Lab Chip 8:2091–2104. doi:10.1039/b814922d

Srigunapalan S, Eydelnant IA, Simmons CA, Wheeler AR (2012) A digital microfluidic platform for primary cell culture and analysis. Lab Chip 12:369–375. doi:10.1039/c1lc20844f

Todd Thorsen SJM, Quake SR (2002) Microfluidic large-scale integration. Science 298:580–584. doi:10.1126/science.1076996

Wei AX, Ge ZX, Zhao XH, Liu J, Zhao Y (2011) Electrical and optical properties of tantalum oxide thin films prepared by reactive magnetron sputtering. J Alloy Compd 509:9758–9763. doi:10.1016/j.jallcom.2011.08.019

Witters D, Knez K, Ceyssens F, Puers R, Lammertyn J (2013) Digital microfluidics-enabled single-molecule detection by printing and sealing single magnetic beads in femtoliter droplets. Lab Chip 13:2047–2054. doi:10.1039/c3lc50119a

Zeng XY, Zhang KD, Pan J, Chen GP, Liu AQ, Fan SK, Zhou J (2013) Chemiluminescence detector based on a single planar transparent digital microfluidic device. Lab Chip 13:2714–2720. doi:10.1039/c3lc50170a